ISSN PRINT 2319 1775 Online 2320 7876

Research paper UGC CARE Listed (Group -I) Journal Volume 11, Iss 8, Dec 2022

Rare Earth Element Cerium Ions Substituted Mn-Ni Spinel Nanoparticles: Enhanced Photocatalytic, Magnetic And Optical Properties

A. Dinesh [1,*], K. Thanrasu[1], K. Kanmani Raja [1,*]

[1] Department of Chemistry, Government Arts College for Men (Autonomous) affiliated to the University of Madras, Nandanam, Chennai – 600035, Tamil Nadu, India

***Corresponding Author:** dineshphdchem@gmail.com (A. Dinesh); kkanmaniraja@gmail.com (K. Kanmani Raja).

ABSTRACT

In this present study, magnetic nanoparticles of $Mn_{0.5}Ni_{0.5}Ce_xFe_{2-x}O_4$ (x = 0, 0.1, 0.3, and 0.5) spinel ferrites were synthesized by a simple combustion method by utilizing the fuel of urea. The formation of a cubic spinel structure was confirmed by powder X-ray diffraction (XRD) performance and the crystallites size was found to be decreased in the range of 24.63 to 15.94 nm with increasing cerium ions. The morphology of $Mn_{0.5}Ni_{0.5}Ce_xFe_{2-x}O_4$ NPs was detected by scanning electron microscope (SEM) and observed sphere shaped nanoparticles, further it was established by high resolution transmission electron microscope (HR-TEM). Energy dispersive X-ray (EDX) studies complete the formation of pure spinel ferrite structure as they ensured the presence of all the elements and the formation of the desired compositions. Furthermore, the bandgap value was estimated to be within 1.38 and 1.75 eV. The appearance of fourier transform infrared (FT-IR) bonds at 440 cm^{-1} is linked to the octahedral (B) metal stretching (Ni-O) and the band at 584 cm^{-1} is connected to the tetrahedral (A) metal stretching (Fe-O), which ensure the formation of $Mn_{0.5}Ni_{0.5}Ce_xFe_{2-x}O_4$ NPs. Magnetic parameters such as remanent (M_r), coercivity (H_c) and saturation magnetization (M_s) were calculated, which exhibited ferromagnetic behavior. The Ms values are decreased with increasing the Ce-doping since the replacement of Fe ions. The photocatalytic (PC) behavior of $Mn_{0.5}Ni_{0.5}Fe_2O_4$, $Mn_{0.5}Ni_{0.5}Ce_{0.1}Fe_{1.9}O_4$, $Mn_{0.5}Ni_{0.5}Ce_{0.3}Fe_{1.7}O_4$ and $Mn_{0.5}Ni_{0.5}Ce_{0.5}Fe_{1.5}O_4$ NPs were analyzed under visible light treatment by the degradation (PCD) of Rhodamine B (RhB) dye. Among the various prepared compositions, $Mn_{0.5}Ni_{0.5}Ce_{0.3}Fe_{1.7}O_4$ exhibits higher PCD efficiency as 94.75 % at 105 min with enhanced visible light absorption range.

Keywords: Ce substituted Mn-Ni ferrite; combustion method; Optical properties; Magnetic properties; Photocatalyst.

1. Introduction

Nanosized spinel ferrites received huge interest due to their low cost, excellent chemical stability, moderate saturation magnetization, high surface area, high specific strength, high wear resistance and low density, low thermal expansion coefficient, and low toxicity to both humans and the environment. These ferrites are promising candidates for a broad range of applications, *i.e.* in magnetic recording media, photoelectric devices, sensors, magnetic pigments,

ISSN PRINT 2319 1775 Online 2320 7876

Research paper UGC CARE Listed (Group -I) Journal Volume 11, Iss 8, Dec 2022

photocatalyst for the dye's degradation, controlled signal transformation, storage devices, batteries, solar cells, etc. [1-5]. Spinel ferrites are the topic of numerous researches due to their magnetic nature and crystalline structure. Minor changes in the size, composition and surface effects convey unique magnetic properties to these ferrites [1].

Metal oxides are widely used in various applications such as in magnetic storage and energy storage device, piezoelectric devices, resistive memory devices, photocatalytic degradation, etc. [1-4]. The cubic spinel structure has a general formula of AB_2O_4 where divalent metal ions A^{2+}= Co^{2+}, Zn^{2+}, Mn^{2+}, Ni^{2+}, etc occupy the tetrahedral (A) sites, and trivalent metal ions B^{3+}= Fe^{3+}, Al^{3+}, etc. occupy the octahedral (B) sites [6]. It is observed that these ferrites exhibited distinct magnetic and physical characteristics upon the alteration of the divalent cations. By rare earth metal ions doping into spinel ferrite structure, the cations distribution between the tetrahedral (A)- and octahedral (B)- sites changes, leading to different magnetic properties. The dopant ion may also change the energy of the grain boundaries, acting as a driving force of the grain growth [7-10].

By altering the divalent cations, it is feasible to obtain expressively different magnetic and physical characteristics in ferrites. The previous studies convey that Ce substituted spinel ferrites exhibit unique characteristics and proved to be versatile magnetic materials widely used in microwave devices, power transformers, read and or write heads for extraordinary speediness digital tape transformers, rod antennas, and gas sensing material [11-13]. When the ferrites are prepared at lower temperatures and the corresponding particle size lies in the nano regime, a difference in the distribution of several ions in the A- and B- sites will be happened [14, 15].

The physico-chemical properties of the nanosized ferrites are strongly influenced by the synthesis route, nature and amount of dopant ion, as well as the presence of structural order-disorder effects [16]. The synthesis route is the crucial factor to obtain high purity nanoferrites [17]. There are several routes to synthesize nanoferrites, such as sol-gel, coprecipitation, refluxing, hydrothermal, mechano-chemical, solid-state, precursor, auto combustion process, microwave plasma, microemulsion, mechanical alloying, etc. [18-20]. Though, the above-stated approaches are found to be costly, tough to synthesis, high budget, time overwhelming and profit was low. Among these synthesis routes, the combustion route is one of the most used approaches for the preparation of ferrite nanocomposites due to its low cost; simplicity; and good control over the structure, physico-chemical, surface and magnetic properties. This method is versatile, simple and effective in producing pure nanoparticles with reduced time and energy.

Precursors of the metal nitrates and the fuel *urea* in a suitable stoichiometric ratio encourage the exothermic and self-sustaining reaction by the combustion process as per the propellant chemistry principle [16-23]. In this paper, $Mn_{0.5}Ni_{0.5}Ce_xFe_{2-x}O_4$ NPs were synthesized through simple combustion technique and be utilizing the fuel urea. The phase, morphological, vibrational, optical, antibacterial activity, magnetic, and photocatalytic characteristics are studied by several physical characterization techniques.

2. Experimental

2.1. Synthesis

Nanoparticles of spinel ferrite of $Mn_{0.5}Ni_{0.5}Ce_xFe_{2-x}O_4$ NPs were synthesized using the corresponding metal nitrates $Mn(NO_3)_2{\cdot}6H_2O$, $Ni(NO_3)_2{\cdot}6H_2O$, $Ce(NO_3)_3{\cdot}6H_2O$, $Fe(NO_3)_3{\cdot}9H_2O$, and the fuel urea. The chemicals were brought from SD fine (India) that were of

ISSN PRINT 2319 1775 Online 2320 7876

Research paper UGC CARE Listed (Group -I) Journal Volume 11, Iss 8, Dec 2022

methodical grade and utilized as received. To prepare the desired compositions, the precursors of metal nitrates of Mn, Ni, Ce and Fe were mixed by maintaining a molar ratio of 1:1:2 and disbanded in double-distilled water. Urea solution was added to the main achieved solutions and stirred for 1 hour. Here, urea works as fuel, whereas the precursors of metal nitrates function as oxidizers.

The obtained solutions were transported into a crucible and were located in microwave ovens (attained from SAMSUNG, India) utilized for the mechanism of irradiation. The yield power was set as 900 Watts for 10 min and the frequency was maintained at 2.54 GHz. Under the influence of ME, the solutions are subjected to the procedures like boiling, vaporization, and finally, decomposition, which result in the production of $Mn_{0.5}Ni_{0.5}Ce_xFe_{2-x}O_4$. Besides, the obtained samples were washed with DI water, ethanol, and then dried at 550 °C for 150 min. The obtained powder products viz. x = 0.0, 0.1, 0.3 and 0.5 were categorized as $Mn_{0.5}Ni_{0.5}Fe_2O_4$, $Mn_{0.5}Ni_{0.5}Ce_{0.1}Fe_{1.9}O_4$, $Mn_{0.5}Ni_{0.5}Ce_{0.3}Fe_{1.7}O_4$ and $Mn_{0.5}Ni_{0.5}Ce_{0.5}Fe_{1.5}O_4$ NPs, respectively.

2.2. Characterization techniques

Powder X-ray diffractometer (Model Rigaku Ultima III) is engaged to confirm the formation of different phases and investigate the crystal structure of obtained $Mn_{0.5}Ni_{0.5}Ce_xFe_{2-x}O_4$ nanoparticles by employing CuKα radiation (λ = 1.5406 Å) and within 2θ range of 20° - 80°. FEI Quanta FEG 200 scanning electron microscope accompanied by energy dispersive X-ray analyzer is utilized to perform the morphological and elemental analysis. The diffuse reflectance spectra were logged in the range of 200-800 nm by utilizing Perkin Elmer (Thermo Scientific Evolution 220) spectrophotometer from which the bandgap value is deduced. Perkin Elmer spectrophotometer (Spectrum RX1) is utilized to log the FTIR spectra. Lake Shore (Model7404, USA,) vibration sample magnetometer (VSM) equipped with 3 magnets is used to perform magnetization measurements at RT.

2.3 Photocatalytic evaluation

The photocatalytic performance of $Mn_{0.5}Ni_{0.5}Fe_2O_4$, $Mn_{0.5}Ni_{0.5}Ce_{0.1}Fe_{1.9}O_4$, $Mn_{0.5}Ni_{0.5}Ce_{0.3}Fe_{1.7}O_4$ and $Mn_{0.5}Ni_{0.5}Ce_{0.5}Fe_{1.5}O_4$ NPs, were examined under visible light (300 W Xenon lamps; λ > 400 nm) irradiation. The photocatalytic activity of the as-prepared samples was analyzed at room temperature (RT). Exactly 100 mg of the photocatalyst was dispersed in 100 mL of Rhodamine B (RhB) (10 mg/L), which was reserved in a quartz glass photocatalytic reactor. Before irradiation, the aliquot was stirred for 30 min in a dark condition and ensured that the catalyst adsorption-desorption equilibrium was attained between the RhB dye and the photocatalyst. The degradation efficiency was examined using UV absorption studies, which lead to determine the dye concentrations at a certain time interval. The catalytic performance of $Mn_{0.5}Ni_{0.5}Fe_2O_4$, $Mn_{0.5}Ni_{0.5}Ce_{0.1}Fe_{1.9}O_4$, $Mn_{0.5}Ni_{0.5}Ce_{0.3}Fe_{1.7}O_4$ and $Mn_{0.5}Ni_{0.5}Ce_{0.5}Fe_{1.5}O_4$ NPs, at various percentages was also investigated.

3. Results and discussion

3.1. Structural analysis

Powder XRD analysis of the as-prepared spinel $Mn_{0.5}Ni_{0.5}Fe_2O_4$, $Mn_{0.5}Ni_{0.5}Ce_{0.1}Fe_{1.9}O_4$, $Mn_{0.5}Ni_{0.5}Ce_{0.3}Fe_{1.7}O_4$ and $Mn_{0.5}Ni_{0.5}Ce_{0.5}Fe_{1.5}O_4$ NPs, are illustrated in **Fig. 1.** From the obtained powder XRD patterns, it is confirmed that the as-prepared samples are well crystalline.

ISSN PRINT 2319 1775 Online 2320 7876

Research paper UGC CARE Listed (Group -I) Journal Volume 11, Iss 8, Dec 2022

The peaks at 2θ values of 18.24˚, 30.13˚, 35.51˚, 37.20˚, 43.23˚, 54.03˚, 57.26˚, 62.92˚ and 75.35˚ are mapped to (111), (220), (311), (222), (400), (422), (511), (440) and (622) reflection planes respectively. The attained diffraction peaks go with diffraction data (JCPDS card number 44-1485), ensuring the establishment of spinel cubic structure with *Fd-3m* space group [24,25].

The crystallite size (L) of the obtained samples was estimated using the (hkl) plane (311) by retaining Debye Scherrer's Eq. (1).

$$L = \frac{0.89\lambda}{\beta \cos\theta} \qquad (1)$$

Where, L, average crystallite size, λ, X-ray source wavelength (0.15406 nm), β, FWHM (full width at half maximum) of the peak; and θ, diffraction angle. The values of the crystallites size deduced for $Mn_{0.5}Ni_{0.5}Ce_xFe_{2-x}O_4$ NPs are established to be within the interval of 24.63 nm to 15.94 nm (**Table 1**).

To deduce the lattice parameter of the $Mn_{0.5}Ni_{0.5}Ce_xFe_{2-x}O_4$ NPs, Eq. 2 was used.

$$a = d_{hkl}\sqrt{(h^2 + k^2 + l^2)} \qquad (2)$$

Where, d_{hkl}, the inter-atomic spacing consistent to the Miller indices h, k, and l of the crystal planes and a, is the lattice parameter. The lattice parameter 'a' value was calculated for $Mn_{0.5}Ni_{0.5}Ce_xFe_{2-x}O_4$ NPs and it was found to be 8.356 Å and 8.398 Å respectively [26]. This increase of 'a' is due to the replacement of larger ionic size Ce cations (0.92 Å) in place of the lower ionic size of Fe cations (0.67 Å) [3]. The ionic radius of Ce^{3+} ion is larger than Fe^{3+} ion, it results a slight expansion of the lattice parameter, which was observed to be in line with Vegard's law.

ISSN PRINT 2319 1775 Online 2320 7876

Research paper UGC CARE Listed (Group -I) Journal Volume 11, Iss 8, Dec 2022

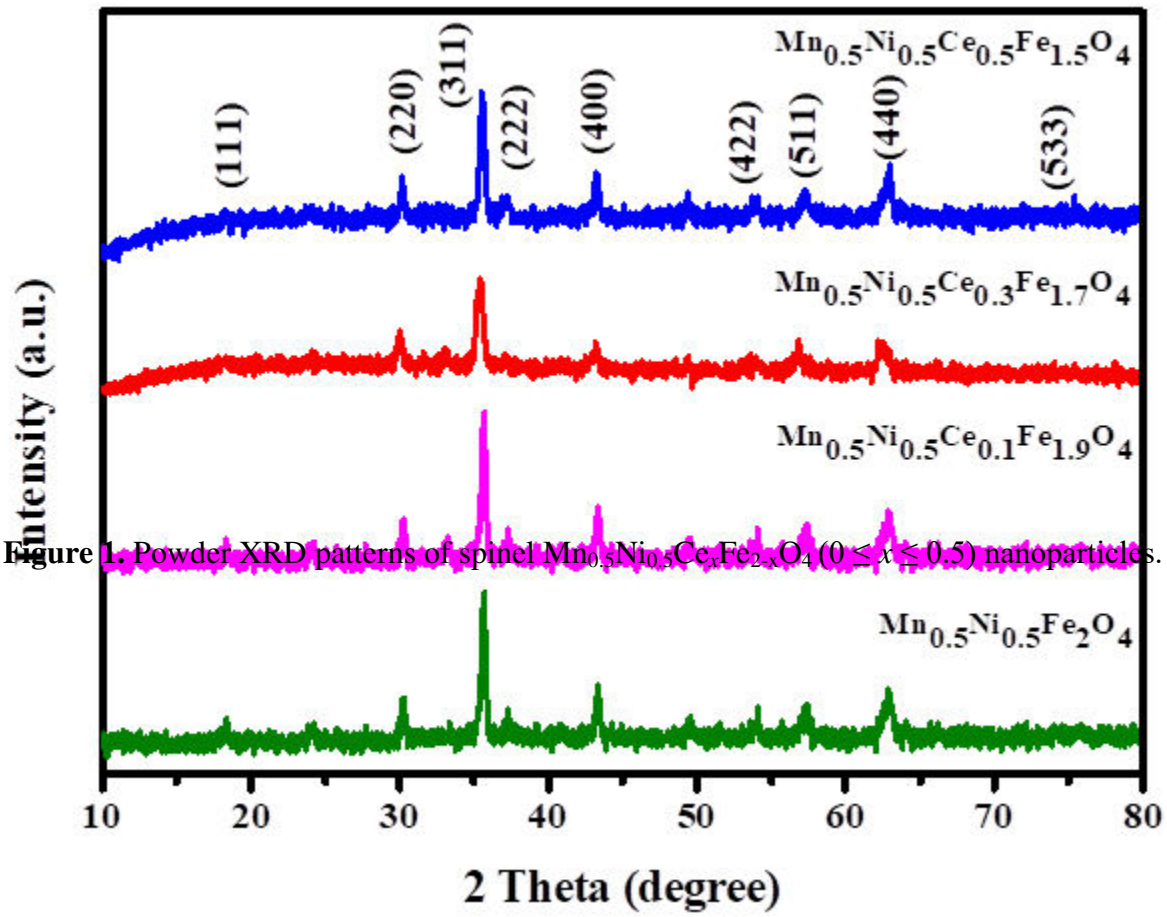

Figure 1. Powder XRD patterns of spinel $Mn_{0.5}Ni_{0.5}Ce_xFe_{2-x}O_4$ ($0 \le x \le 0.5$) nanoparticles.

Table 1. Crystallite size (L) and lattice parameter (a) and energy gap (Eg) of spinel $Mn_{0.5}Ni_{0.5}Ce_xFe_{2-x}O_4$ ($0 \le x \le 0.5$) nanoparticles.

Sample compositions	*L* (nm) by Debye Scherrer	*D* (nm) by William-Hall plot	*a* (Å)	Energy gap, E_g (eV)
$Mn_{0.5}Ni_{0.5}Fe_2O_4$	24.63	25.33	8.356	1.38
$Mn_{0.5}Ni_{0.5}Ce_{0.1}Fe_{1.9}O_4$	22.48	24.21	8.374	1.51
$Mn_{0.5}Ni_{0.5}Ce_{0.3}Fe_{1.7}O_4$	15.94	17.64	8.383	1.69
$Mn_{0.5}Ni_{0.5}Ce_{0.5}Fe_{1.5}O_4$	18.56	19.52	8.398	1.75

ISSN PRINT 2319 1775 Online 2320 7876

Research paper UGC CARE Listed (Group -I) Journal Volume 11, Iss 8, Dec 2022

The effective size of the crystallite (D) is also obtained by employing Williamson-Hall (W-H) plot equation:

$$\frac{\beta\cos\theta}{\lambda} = \frac{k}{D} + \frac{4\varepsilon\sin\theta}{\lambda} \quad (3)$$

0.89, the value of constant k, and the strain associated with samples is represented by ε. Fig. 2 shows the W-H plots (i.e. βcosθ/λ vs 4sinθ/λ) where the intercept (k/D) is used to determine the actual crystallite size (D) of $Mn_{0.5}Ni_{0.5}Ce_xFe_{2-x}O_4$ NPs. It is observed that the crystallites size obtained by W-H method is lesser in comparison with the crystallites size deduced by Debye Scherer's method. The variance is mainly due to the contribution of the strain module in the W-H plot. With an increase in Ce content (x), the crystallite size shrinkages, while an increase in the lattice parameter was observed [27]. For instance, the reduction in crystallites size with Ce doping could be attributed to the reason that the Ce^{3+} ions display large ionic radii and hence show limited solubility in spinel lattice and inhibits the grain growth.

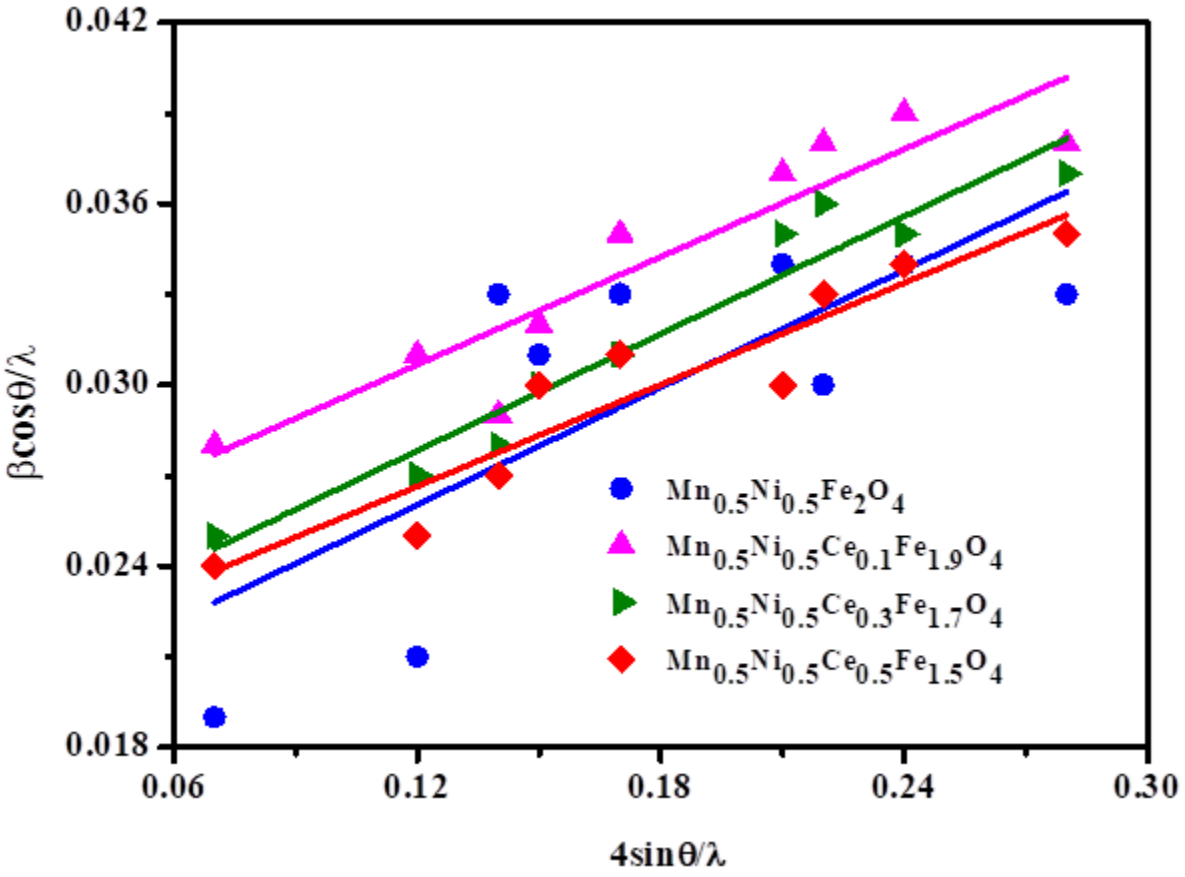

Figure 2. W-H plots of spinel $Mn_{0.5}Ni_{0.5}Ce_xFe_{2-x}O_4$ ($0 \le x \le 0.5$) nanoparticles

3.2 SEM analysis

The surface morphology studies of the $Mn_{0.5}Ni_{0.5}Ce_xFe_{2-x}O_4$ NPs were performed with the aid of SEM. The obtained SEM images illustrated a spherical morphology and also revealed joining

ISSN PRINT 2319 1775 Online 2320 7876

Research paper UGC CARE Listed (Group -I) Journal Volume 11, Iss 8, Dec 2022

and agglomerated grains as shown in **Fig. 3a-d**. The agglomerated and spherical morphology was noticed in the different $Mn_{0.5}Ni_{0.5}Ce_xFe_{2-x}O_4$ (x = 0.0 to 0.5) NPs, which is mostly due to the lower microwave energy release during the evolution of combustion [28].

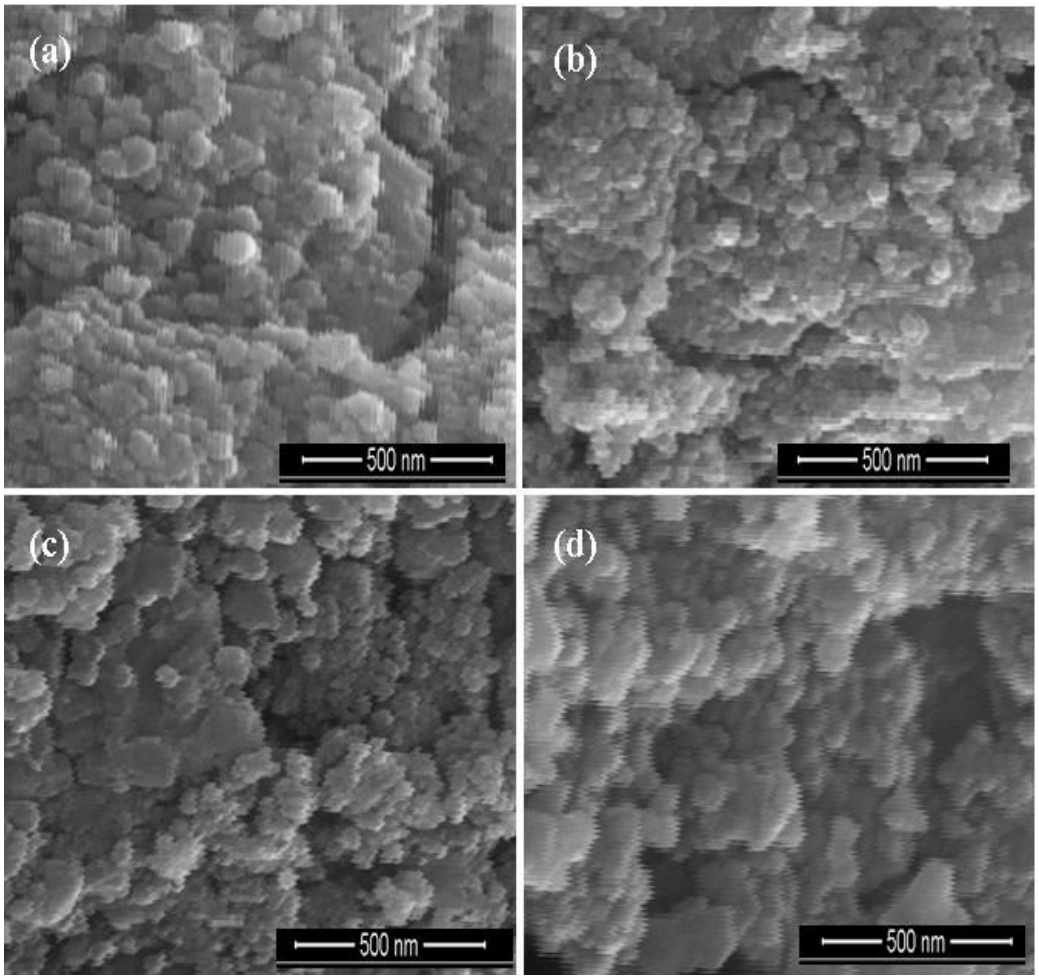

Figure 3. HR-SEM images of (a) $Mn_{0.5}Ni_{0.5}Fe_2O_4$, (b) $Mn_{0.5}Ni_{0.5}Ce_{0.1}Fe_{1.9}O_4$, (c) $Mn_{0.5}Ni_{0.5}Ce_{0.3}Fe_{1.7}O_4$ and (d) $Mn_{0.5}Ni_{0.5}Ce_{0.5}Fe_{1.5}O_4$ NPs.

3.3 HR-TEM analysis

To find further evidence on the nano-scaled fine structure of $Mn_{0.5}Ni_{0.5}Ce_xFe_{2-x}O_4$ (x = 0, 0.1, 0.3 to 0.5) NPs, a essential analysis was achieved by HR-TEM as revealed in **Fig. 4a-d**, respectively. The HR-TEM images of the samples clearly showed that spherical-shaped particles like nanostructures with a particle size smaller than 50 nm are formed. The TEM images reveal irregular shape particles that form agglomerates. As a result of the doping with Ce ions, the particle size decrease from 30 nm ($Mn_{0.5}Ni_{0.5}Fe_2O_4$), 28 nm ($Mn_{0.5}Ni_{0.5}Ce_{0.1}Fe_{1.9}O_4$), 24nm ($Mn_{0.5}Ni_{0.5}Ce_{0.3}Fe_{1.7}O_4$) and 20 nm ($Mn_{0.5}Ni_{0.5}Ce_{0.5}Fe_{1.5}O_4$), respectively. The particle

ISSN PRINT 2319 1775 Online 2320 7876

Research paper UGC CARE Listed (Group -I) Journal Volume 11, Iss 8, Dec 2022

agglomeration is frequently observed in case of the samples synthesized by thisroutes and is caused most probably by the assembling tendency of small particles, magnetic nature and weak surface interaction due to Van der Waals forces [22]. The internal heat energy produced during annealing may also led to the agglomeration of particles due to interfacial surface friction [4]. Crystallographic clarifications of the as-prepared sample were done by recording the SAED (selected area electron diffraction) outlines of $Mn_{0.5}Ni_{0.5}Ce_{0.3}Fe_{1.7}O_4$ NPs as shown in Fig. 4a-d (insets). A set of significant Debye rings agreeing to *hkl* planes; 311, 400, 511, and 440 of cubic crystal structure indexed a test of the purity and crystallinity of the products. The Debye rings appeared as incessant and are diffused and also evidently visible, agreement to good crystallinity, which additional leaflets that the products are very much in the nano regime and well-developed nanoparticles

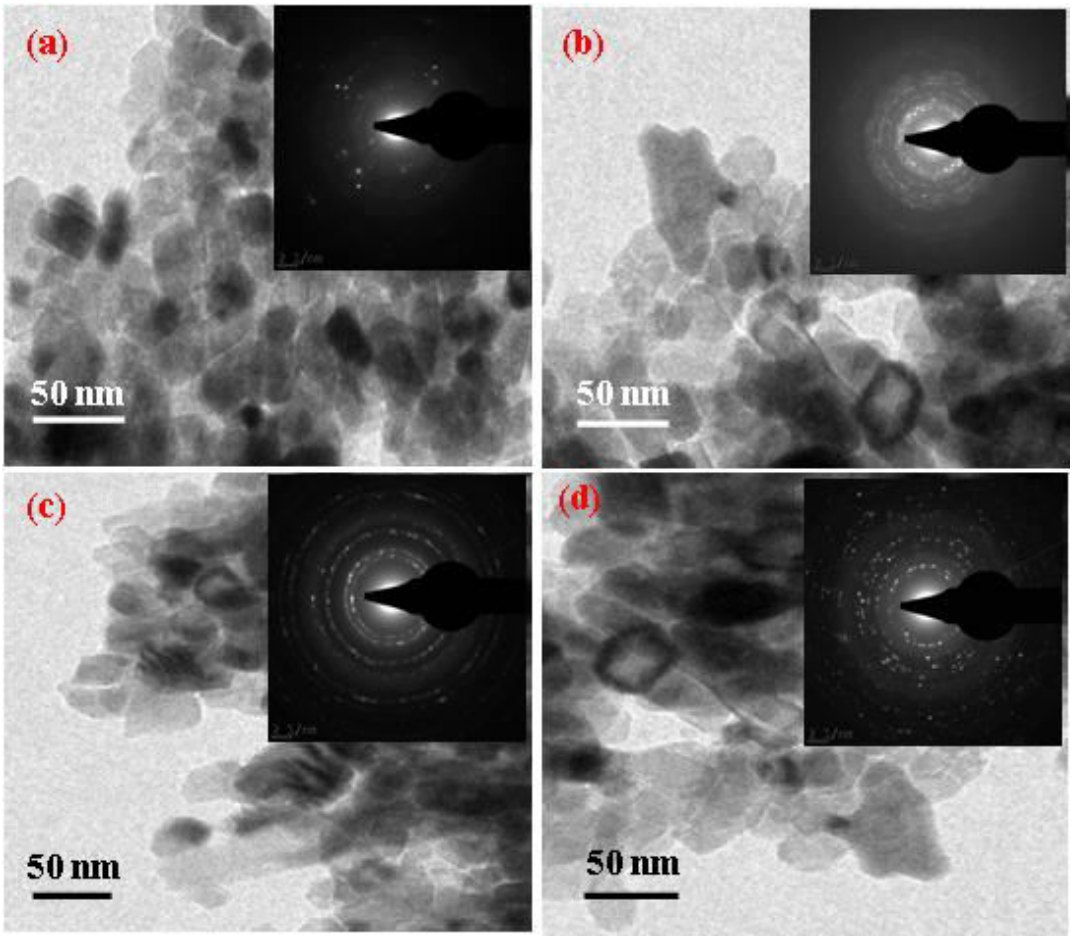

Figure 4. HR-TEM images of (a) $Mn_{0.5}Ni_{0.5}Fe_2O_4$, (b) $Mn_{0.5}Ni_{0.5}Ce_{0.1}Fe_{1.9}O_4$, (c) $Mn_{0.5}Ni_{0.5}Ce_{0.3}Fe_{1.7}O_4$ and (d) $Mn_{0.5}Ni_{0.5}Ce_{0.5}Fe_{1.5}O_4$ NPs. SAED patterns of respective samples.

ISSN PRINT 2319 1775 Online 2320 7876

Research paper UGC CARE Listed (Group -I) Journal Volume 11, Iss 8, Dec 2022

3.4. Optical band gap analysis

To study the optical and bandgap features of $Mn_{0.5}Ni_{0.5}Ce_xFe_{2-x}O_4$ NPs, UV-Vis diffuse reflectance spectra (DRS) is used. Energy band gap was determined with aid of Tauc plots. Kubelka–Munk (K-M) function F(R) is utilized to transform the diffused reflectance into absorption co-efficient, as stated in equation (4).

$$\alpha = F(R) = \frac{(1-R)^2}{2R} \quad (4)$$

Where, α the absorption coefficient and R reflectance. Therefore, the Tauc relation can be stated in equation (5),

$$F(R)h\nu = A(h\nu - E_g)^n \quad (5)$$

Where A, ν, h, and E_g, absorption coefficient, light frequency, Plank's constant and bandgap respectively. The permitted direct and indirect transitions are denoted by n = 2 and ½., from where the values of both direct as well as indirect bandgap are obtained.

The intention of the band-gap energy contains the extrapolation of the linear part of the curve attained by plotting $(F(R)h\nu)^2$ versus hν to overlap the energy axis for all compositions (**Fig. 5**). Bandgap values can be assumed by extrapolation of the direct locations in the Tauc plot $(F(R)h\nu)^2$ [29, 30]. The estimated energy band gap values were found to be 1.38, 1.51, 1.69, and 1.75 eV for x = 0.0, 0.1, 0.3, and 0.5, respectively (Table 1) [31]. The variations of the optical bandgap due to the defects, additional sub-band energy molded by substation of Ce^{3+} ions and crystallite size of the nanoparticles [32]. For instance, the decline in bandgap energy with Ce substitution could be also ascribed to the increase in the concentration of impurity phase.

ISSN PRINT 2319 1775 Online 2320 7876

Research paper UGC CARE Listed (Group -I) Journal Volume 11, Iss 8, Dec 2022

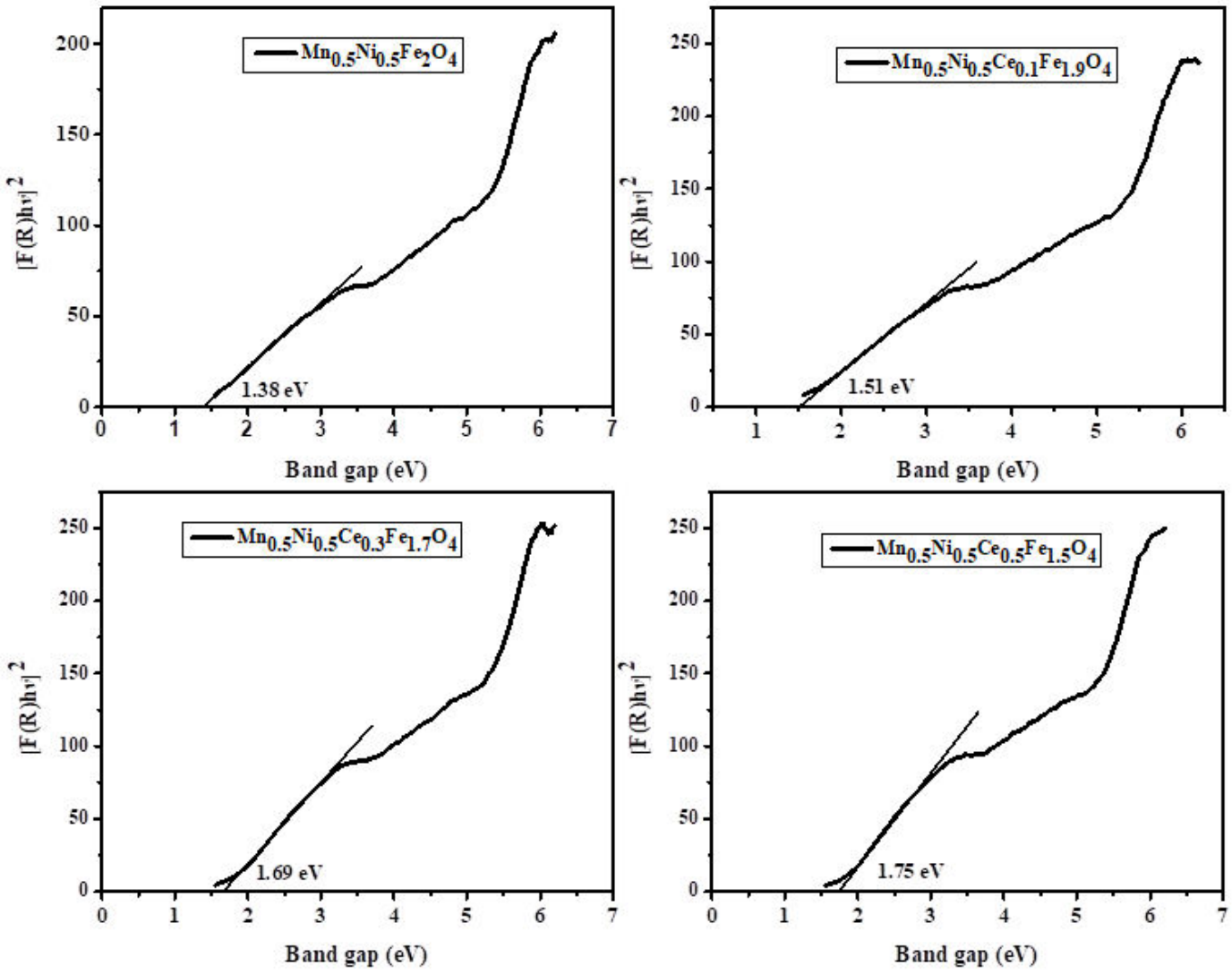

Figure 5. $(F(R)h\upsilon)^2$ versus *hv* plots of $Mn_{0.5}Ni_{0.5}Fe_2O_4$, $Mn_{0.5}Ni_{0.5}Ce_{0.1}Fe_{1.9}O_4$, $Mn_{0.5}Ni_{0.5}Ce_{0.3}Fe_{1.7}O_4$ and $Mn_{0.5}Ni_{0.5}Ce_{0.5}Fe_{1.5}O_4$ NPs.

3.5 FTIR spectral analysis

FT-IR spectra of $Mn_{0.5}Ni_{0.5}Ce_xFe_{2-x}O_4$ NPs are showed in **Fig. 6**. The FT-IR spectra were registered in the range of 4000-400 cm^{-1} at RT. The broadband at 3435 cm^{-1} is linked to H-O stretching [33]. The C-H stretching vibration is connected with the band at 2925 and 2853 cm^{-1} [4]. The specific absorption bands at 1643 and 1434 cm^{-1} are assigned to the C-O stretching band, due to the occurrence of organic species (e.g. COO^-) on the particle surface [34]. The bands at 1109, 1029 cm^{-1} are related with the vibrations of the spinel structure of $Mn_{0.5}Ni_{0.5}Ce_xFe_{2-x}O_4$ NPs [35]. The bonds at 440, 584 cm^{-1}, is consigned to B-metal stretching (Mn-O; Ni-O) and 859 cm^{-1} are connected to the A- metal stretching (Fe-O) [36].

ISSN PRINT 2319 1775 Online 2320 7876

Research paper UGC CARE Listed (Group -I) Journal Volume 11, Iss 8, Dec 2022

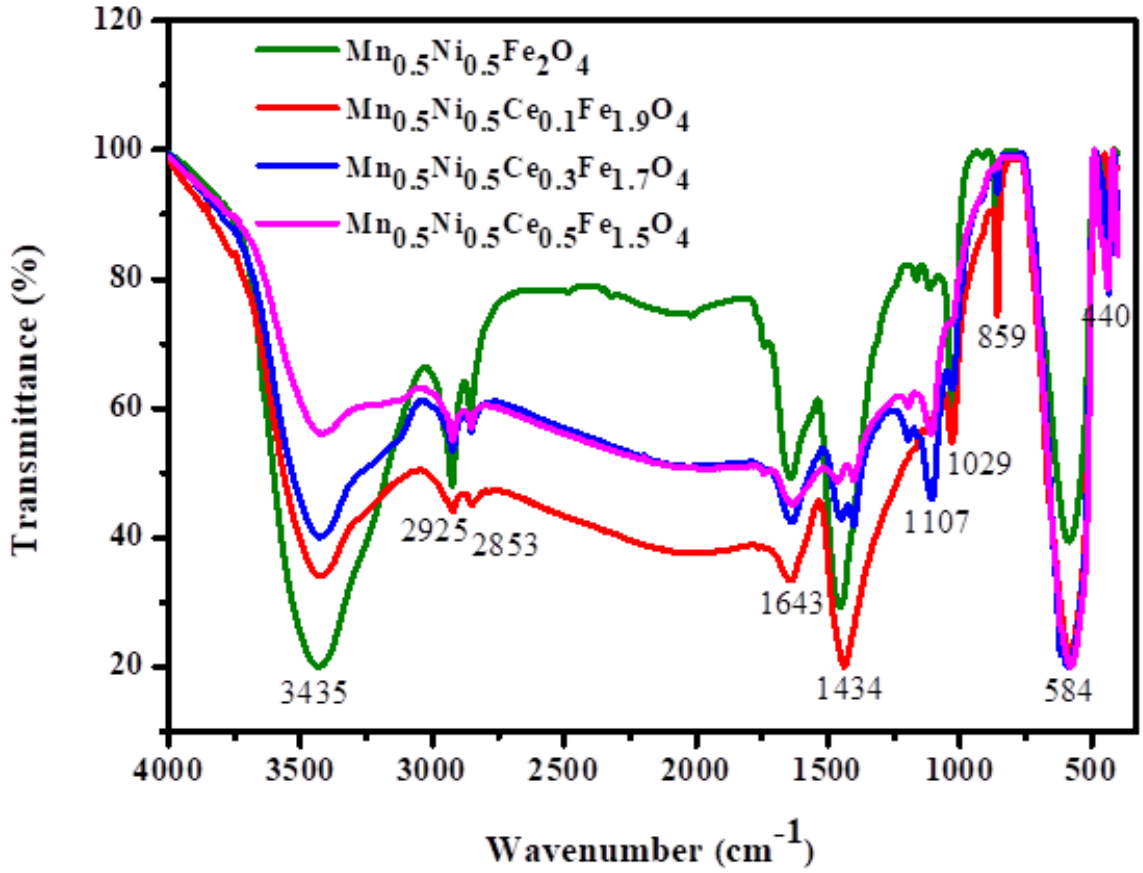

Figure 6. FTIR spectra of spinel (a) $Mn_{0.5}Ni_{0.5}Fe_2O_4$, (b) $Mn_{0.5}Ni_{0.5}Ce_{0.1}Fe_{1.9}O_4$, (c) $Mn_{0.5}Ni_{0.5}Ce_{0.3}Fe_{1.7}O_4$ and (d) $Mn_{0.5}Ni_{0.5}Ce_{0.5}Fe_{1.5}O_4$ NPs.

3.6. Magnetization analysis

The magnetic parameters of $Mn_{0.5}Ni_{0.5}Ce_xFe_{2-x}O_4$ NPs were undertaken at room temperature and a stimulated magnetic field of -15 to +15 kOe. The magnetization (M) vs. applied field (H) plots is used to measure the saturation magnetization (M_s), coercivity (H_c), and remanence (M_r) was determined. $Mn_{0.5}Ni_{0.5}Ce_xFe_{2-x}O_4$ NPs exhibited normal spinel structure, as divalent (Mn^{2+} and Ni^{2+}) and trivalent (Ce^{3+}/Fe^{3+}) metal ions reside in A and B sites [7, 8] and was found to exhibit ferromagnetic. All samples display ferromagnetic behavior with well-defined hysteresis loops; however, significant changes in the magnetic parameters are induced by the doping ions. Small size particles contain less domain walls and require higher demagnetization force, while larger size particles have higher probability of domain formation [8]. The H_c of $Mn_{0.5}Ni_{0.5}Ce_xFe_{2-x}O_4$ NPs were found to lie within 270.86 Oe to 398.58 Oe (**Fig. 7** and **Table 2**). The coercivity value is primarily organized by factors such as high anisotropy and cationic rearrangement [1, 2]. Costa *et al.* reported superparamagnetic behavior whereas in this work ferromagnetic nature is observed. Hence, H_c values reported here is an order of magnitude smaller than those given in

ISSN PRINT 2319 1775 Online 2320 7876

Research paper UGC CARE Listed (Group -I) Journal Volume 11, Iss 8, Dec 2022

[5]. From the M-H hysteresis loop M_r values for $Mn_{0.5}Ni_{0.5}Ce_xFe_{2-x}O_4$ NPs was found to be 8.15 emu/g (x= 0.0), 6.83 emu (x= 0.1) and 5.92 emu/g (x= 0.3), then M_r values declined to 5.54 emu/g for (x= 0.5), whose values are found to be reliant on the crystallite size and shape of $Mn_{0.5}Ni_{0.5}Fe_2O_4$ NPs [8]. From the M-H loop, M_s values for cerium ions doping $Mn_{0.5}Ni_{0.5}Ce_xFe_{2-x}O_4$ NPs were found to be within 31.23 emu/g to 17.75 emu/g.

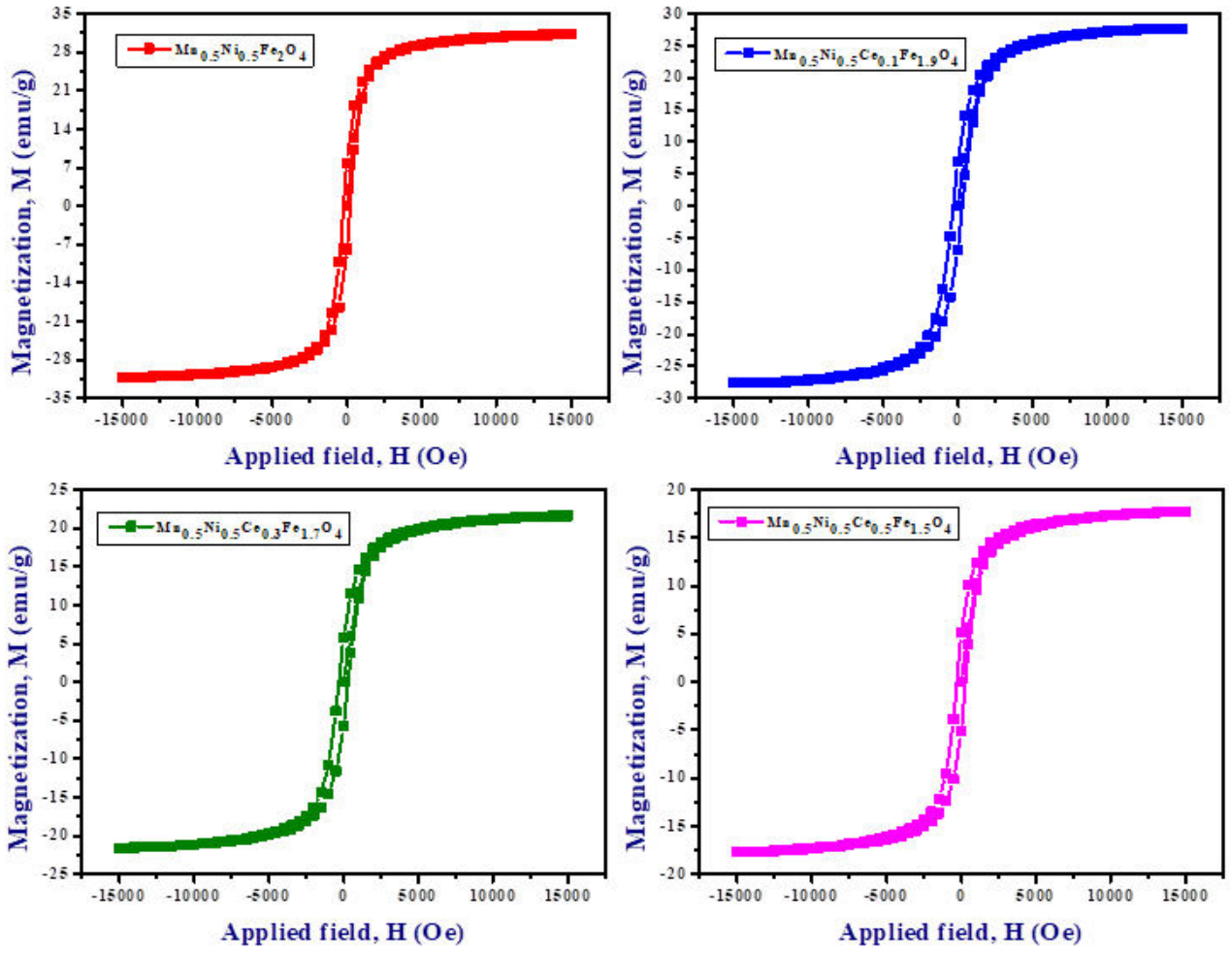

Sample Name	H_c, (O_e)	M_r (emu/g)	M_s (emu/g)
$Mn_{0.5}Ni_{0.5}Fe_2O_4$	270.86	8.12	31.23
$Mn_{0.5}Ni_{0.5}Ce_{0.1}Fe_{1.9}O_4$	320.78	6.83	27.84
$Mn_{0.5}Ni_{0.5}Ce_{0.3}Fe_{1.7}O_4$	358.65	5.92	21.57
$Mn_{0.5}Ni_{0.5}Ce_{0.5}Fe_{1.5}O_4$	398.47	5.47	17.75

ISSN PRINT 2319 1775 Online 2320 7876

Research paper UGC CARE Listed (Group -I) Journal Volume 11, Iss 8, Dec 2022

Figure 7. M-H hysteresis loops of spinel $Mn_{0.5}Ni_{0.5}Ce_xFe_{2-x}O_4$ ($0 \leq x \leq 0.5$) nanoparticles.

Table 2. Coercivity, remanant magnetization, saturation magnetization of spinel $Mn_{0.5}Ni_{0.5}Ce_xFe_{2-x}O_4$ ($0 \leq x \leq 0.5$) NPs.

3.7.

Photocatalytic studies

$Mn_{0.5}Ni_{0.5}Ce_xFe_{2-x}O_4$ NPs were examined towards the adsorption-desorption equilibrium that was achieved in 30 min and towards the photocatalytic dye degradation (PCD) of Rhodamine B (RhB) below visible light irradiation [37, 38]. The PCD efficiency rates of C/C_0 (%) vs. time for RhB were shown in **Fig. 8**. The photocatalytic constancy of the blank solution under visible light irradiation was calculated in the nonappearance of $Mn_{0.5}Ni_{0.5}Ce_xFe_{2-x}O_4$ NPs over 105 min, resulting in a PCD efficiency of 6.54%. The PCD efficiency of RhB solution using $Mn_{0.5}Ni_{0.5}Ce_{0.3}Fe_{1.7}O_4$ NPs showed a higher degradation percentage (94.75%) than other samples. It was initiate that the UV-adsorption intensity of RhB decreased with the increase of the reaction time progressively. All the degradation measurement values are offered in **Table 3.**

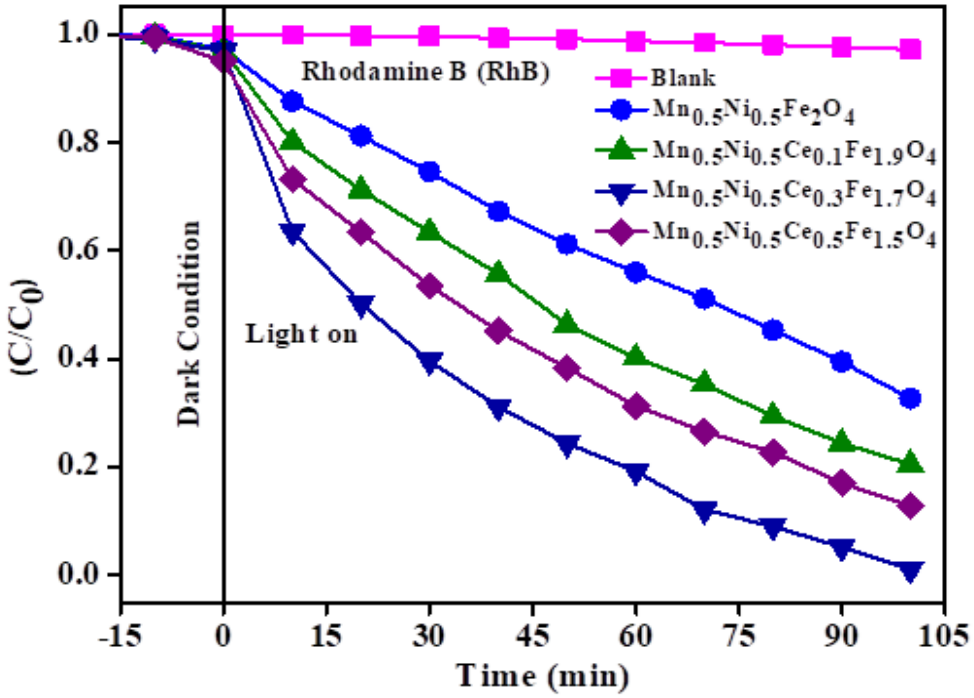

ISSN PRINT 2319 1775 Online 2320 7876

Research paper UGC CARE Listed (Group -I) Journal Volume 11, Iss 8, Dec 2022

Figure 8. Rhodamine B dye degradation using spinel $Mn_{0.5}Ni_{0.5}Ce_xFe_{2-x}O_4$ ($0 \leq x \leq 0.5$) nanoparticles

Table 3. Percentage degradation of Rhodamine B on to $Mn_{0.5}Ni_{0.5}Ce_xFe_{2-x}O_4$ ($0 \leq x \leq 0.5$) NPs

Sample	RhB dye degradation efficiency (%)
Blank	6.24
$Mn_{0.5}Ni_{0.5}Fe_2O_4$	59.22
$Mn_{0.5}Ni_{0.5}Ce_{0.1}Fe_{1.9}O_4$	82.44
$Mn_{0.5}Ni_{0.5}Ce_{0.3}Fe_{1.7}O_4$	94.75
$Mn_{0.5}Ni_{0.5}Ce_{0.5}Fe_{1.5}O_4$	87.94

3.8. Kinetic studies

The kinetics rate of RhB dye photocatalytic decomposition study of $Mn_{0.5}Ni_{0.5}Ce_xFe_{2-x}O_4$ NPs catalyst surface can be signified by the -pseudo-first-order equation:.

$$-\ln(Ct/C_0) = k_{abs}(t) \quad (6)$$

Where, Ct = concentration of RhB at various time (t), C_0 = initial dye concentration and kabs = pseudo-first order rate constant of dye removal (**Fig. 9**) and noted that $Mn_{0.5}Ni_{0.5}Ce_{0.3}Fe_{1.7}O_4$ NPs possesses higher rate constant than other compositions [38]. Hence, spinel $Mn_{0.5}Ni_{0.5}Ce_{0.3}Fe_{1.7}O_4$ NPs is the optimal attentiveness to enhance the PCD of RhB. The rate constant k_{abs} value of RhB from the experimental data was given in **Table 4.**

Table 4. Rate constant k_{abs} value for the degradation of Rhodamine B (RhB) on to spinel $Mn_{0.5}Ni_{0.5}Ce_xFe_{2-x}O_4$ ($0 \leq x \leq 0.5$) NPs

Samples	k min^{-1}				
	Blank	$Mn_{0.5}Ni_{0.5}Fe_2O_4$	$Mn_{0.5}Ni_{0.5}Ce_{0.1}Fe_{1.9}O_4$	$Mn_{0.5}Ni_{0.5}Ce_{0.3}Fe_{1.7}O_4$	$Mn_{0.5}Ni_{0.5}Ce_{0.5}Fe_{1.5}O_4$
RhB	0	0.0046	0.0135	0.0189	0.0149

ISSN PRINT 2319 1775 Online 2320 7876

Research paper UGC CARE Listed (Group -I) Journal Volume 11, Iss 8, Dec 2022

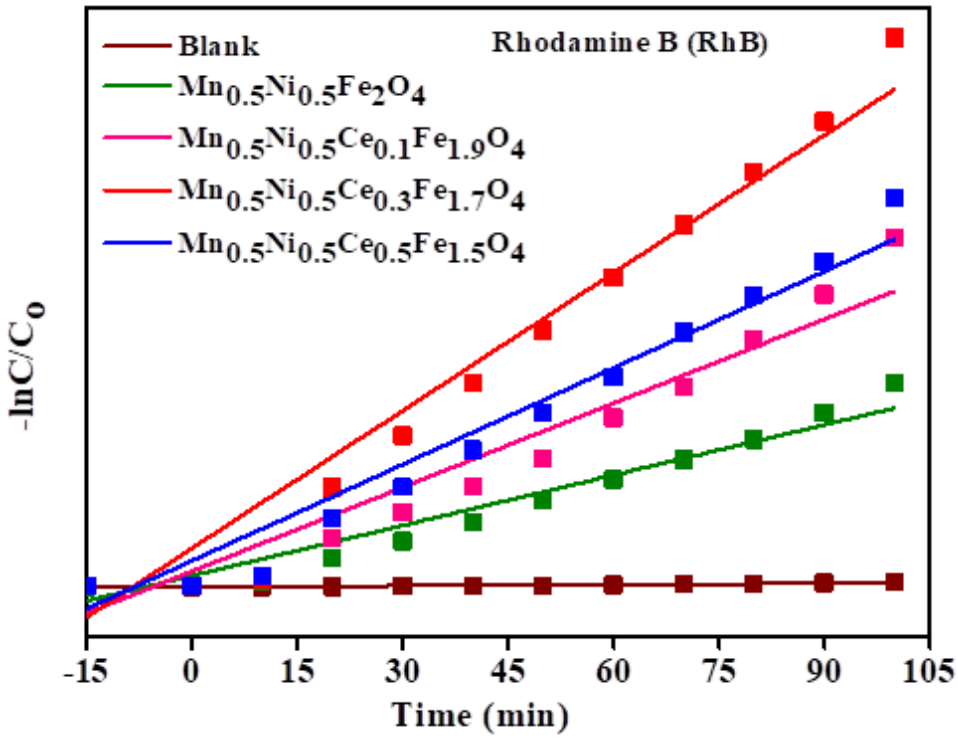

Figure 9. Pseudo first-order kinetic plot for Rhodamine B dye degradation using spinel $Mn_{0.5}Ni_{0.5}Ce_xFe_{2-x}O_4$ ($0 \leq x \leq 0.5$) nanoparticles.

3.9. Photocatalytic degradation mechanism

Based on the above outcomes and discussions, an appropriate photocatalytic degradation mechanism for RhB degradation over $Mn_{0.5}Ni_{0.5}Ce_xFe_{2-x}O_4$ NPs is discussed herein. When passing the visible light on the catalysts surface, the electrons (e^-) get excited from VB (valence band) to CB (conduction band) of $Mn_{0.5}Ni_{0.5}Ce_xFe_{2-x}O_4$ NPs along with producing holes (h^+) in the VB. The CB excited electrons of $Mn_{0.5}Ni_{0.5}Ce_xFe_{2-x}O_4$ NPs get combined Cerium and electron-hole pair recombination rates become lower, hence enhances the photocatalytic process [38]. The CB electron get combines with a dissolved oxygen molecule to form anions of peroxide radicals ($\bullet O_2^-$) and similarly created hydroxyl radicals (•OH), owing to the reaction amongst holes and OH− ions. The RhB decomposes into a simpler molecule in the presence of •OH and $\bullet O_2^-$ species into CO_2 and H_2O. The appropriate PCD mechanism is listed in the equation.

$$Mn_{0.5}Ni_{0.5}Fe_2O_4 + \text{Visible Light } (h\nu) \longrightarrow h^+(VB) + e^- (CB) \quad (2)$$

$$h^+_{(VB)} + H_2O \longrightarrow H^+ + \bullet OH \quad (3)$$

$$e^- + O_2 \longrightarrow \bullet O_2^- \quad (4)$$

$$[\text{RhB Dye}] + \bullet O_2^- + \bullet OH \longrightarrow H_2O + CO_2 \quad (5)$$

4. Conclusions

ISSN PRINT 2319 1775 Online 2320 7876

Research paper UGC CARE Listed (Group -I) Journal Volume 11, Iss 8, Dec 2022

Magnetic nanoparticles of $Mn_{0.5}Ni_{0.5}Ce_xFe_{2-x}O_4$ NPs were prepared by simple combustion method and by utilizing the fuel urea. XRD established the cubic spinel structure with space group *Fd-3m*. The lattice parameter (a) values were found to be in 8.356 Å to 8.398 Å intervals. The surface morphology, structure, phase purity, and crystallinity were confirmed by HR-SEM, HR-TEM, and SAED patterns. The bandgap values were observed to lie within 3.39-3.26 eV interval attained by using the optical absorption spectra. FT-IR unveils the existence of all the characteristic functional groups of $Mn_{0.5}Ni_{0.5}Ce_xFe_{2-x}O_4$ NPs spinel nanoparticles. M_s values for $Mn_{0.5}Ni_{0.5}Ce_xFe_{2-x}O_4$ NPs were deduced and it is observed to lie within 31.23 to 17.75 emu/g respectively. The M_r values are strongly reliant on the crystallite size and shape. The photocatalytic degradation efficiency of Rhodamine B using $Mn_{0.5}Ni_{0.5}Ce_xFe_{2-x}O_4$ NPs under visible light. The photocatalyst $Mn_{0.5}Ni_{0.5}Ce_{0.3}Fe_{1.7}O_4$ NPs exhibits higher photocatalytic degradation efficiency as 93.88 % at 105 min was attained successfully and it may apply for the environmental pollution remediation process.

References

[1] M. A. Almessiere, Y. Slimani, S. Güner, A. Baykal, I Ercan, Effect of dysprosium substitution on magnetic and structural properties of $NiFe_2O_4$ nanoparticles, Journal of Rare Earths 37(8) (2019) 871-878.

[2] A. Kale, S. Gubbala, R.D.K. Misra, Magnetic behavior of nanocrystalline nickel ferrite synthesized by the reverse micelle technique, J. Magn. Magn. Mater. 277 (2004) 350–358.

[3] Y Slimani, A Baykal, A Manikandan, Effect of Cr^{3+} substitution on AC susceptibility of Ba hexaferrite nanoparticles, J. Magn. Magn. Mater. 458 (2018) 204-212.

[4] A.C.F.M. Costa, V.J. Silva, D.R. Cornejo, M.R. Morelli, R.H.G.A. Kiminami, L. Gama, Magnetic and structural properties of $NiFe_2O_4$ ferrite nanopowder doped with Zn^{2+}, J. Magn. Magn. Mater. 320 (2008) 370.

[5] V.D. Kapse, S.A. Ghosh, F.C. Raghuwanshi, S.D. Kapse, Nanocrystalline spinel $Ni_{0.6}Zn_{0.4}Fe_2O_4$: A novel material for H_2S sensing, Mater. Chem. Phys. 113 (2009) 638–644.

[6] V.D. Kapse, S.A. Ghosh, F.C. Raghuwanshi, S.D. Kapse, U.S. Khandekar, Nanocrystalline $Ni_{0.6}Zn_{0.4}Fe_2O_4$: A novel semiconducting material for ethanol detection, Talanta 78 (2009) 19–25.

[7] H. Albetran, Y. Slimani, M.A.Almessiere, F. Alahmari, Sagar E. Shirsath, S. Akhtar, I.M. Low, A. Baykal, I. Ercan, Synthesis, characterization and magnetic investigation of Er-substituted electrospun $NiFe_2O_4$ nanofibers, Physica Scripta 95(7) (2020) 075801.

[8] J.P. Chen, C.M. Sorenson, K.J. Klabunde, G.C. Hadjipanayis, E. Devlin, A. Kostikas, Size-dependent magnetic properties of $MnFe_2O_4$ fine particles synthesized by coprecipitation, Phys. Rev. B 54 (1996) 9288–9296.

[9] A. Manikandan, S. Arul Antony, R. Sridhar, Seeram Ramakrishna, M. Bououdina, A simple combustion synthesis and optical studies of magnetic $Zn_{1-x}Ni_xFe_2O_4$ nanostructures for photoelectrochemical applications, J. Nanosci. Nanotechnol. 15 (2015) 4948-4960.

[10] M. Srivastava, S. Chaubey, Animesh K. Ojha, Investigation on size dependent structural and magnetic behavior of nickel ferrite nanoparticles prepared by sol-gel and hydrothermal methods, Mater. Chem. Phys. 118 (2009) 174-180.

[11] J. Wang, F. Ren, R. Yi, A. Yan, G. Qiu, X. Liu, Solvothermal synthesis and magnetic properties of size-controlled nickel ferrite nanoparticles, J. Alloys Compds. 479 (2009) 791-796.

ISSN PRINT 2319 1775 Online 2320 7876

Research paper UGC CARE Listed (Group -I) Journal Volume 11, Iss 8, Dec 2022

[12] Manoj M. Kothawale, R. B. Tangsali, G. K. Naik and J. S. Budkuley, Characterization and Magnetic Properties of Nanoparticle $Ni_{1-x}Zn_xFe_2O_4$ Ferrites Prepared Using Microwave Assisted Combustion Method, J. Supercond. Nov. Magn. 25 (2012) 1907-1911.

[13] S. Mirzaee, Y.A. Kalandaragh, P. Rahimzadeh, Modified co-precipitation process effects on the structural and magnetic properties of Mn- doped nickel ferrite nanoparticles, Solid State Sci. 99 (2020) 106052 (1-6).

[14] G. Nabiyouni, M. Jafari Fesharaki, M. Mozafari and J. Amighian, Characterization and Magnetic Properties of Nickel Ferrite Nanoparticles Prepared by Ball Milling Technique, Chinese Phys. Lett. 27 (2010) 12.

[15] A. Manikandan, R. Sridhar, S. Arul Antony, S. Ramakrishna, A simple aloe vera plant-extracted microwave and conventional combustion synthesis: Morphological, optical and catalytic properties of magnetic $CoFe_2O_4$ nanostructures, J. Mol. Struct. 1076 (2014) 188-200.

[16] A. Manikandan, M. Durka, M. A. Selvi, S. Arul Antony, Sesamum indicum plant extracted microwave combustion synthesis and opto-magnetic properties of spinel $Mn_xCo_{1-x}Al_2O_4$ nano-catalysts, J. Nanosci. Nanotech. 16 (2016) 448-456.

[17] A. Manikandan, M. Durka, S. Arul Antony, Hibiscus rosa-sinensis leaf extracted green methods, magneto-optical and catalytic properties of spinel $CuFe_2O_4$ nano- and microstructures, J. Inorg. Organomet. Polym. 15 (2015) 1019–1031.

[18] A. Manikandan, M. Durka, M. A. Selvi, S. Arul Antony, Aloe vera plant extracted green synthesis, structural and opto-magnetic characterizations of spinel $Co_xZn_{1-x}Al_2O_4$ nano-catalysts, J. Nanosci. Nanotech. 16 (2016) 357-373.

[19] S. Asiri, M. Sertkol, H. Gungunes, Md Amir, A. Manikandan, I. Ercan, A. Baykal, The temperature effect on magnetic properties of $NiFe_2O_4$ nanoparticles, J. Inorg. Organomet. Polym. 28 (2018) 1587–1597.

[20] P. Bhavani, A. Manikandan, P. Paulraj, A. Dinesh, M. Durka, and S. Arul Antony, Okra (Abelmoschus esculentus) Plant Extract-Assisted Combustion Synthesis and Characterization Studies of Spinel $ZnAl_2O_4$ Nano-Catalysts, J. Nanosci. Nanotech. 18 (2018) 4072–4081.

[21] S. Jayasree, A. Manikandan, A. M. Uduman Mohideen, C. Barathiraja, S. Arul Antony, Comparative study of combustion methods, opto-magnetic and catalytic properties of spinel $CoAl_2O_4$ nano- and microstructures, Adv. Sci., Eng. Med. 7 (2015) 672-682.

[22] A. Manikandan, S. Arul Antony, A novel approach for the synthesis and characterization studies of Mn^{2+} doped CdS nano-crystals by a facile microwave combustion method, J. Supercond. Nov. Magn. 27 (2014) 2725-2733.

[23] S. Moortheswaran, A. Manikandan, S. Sujatha, S. K. Jaganathan, S. Arul Antony, Selective catalytic oxidation of benzyl alcohol and characterization studies of spinel $MnAl_2O_4$ nanoparticles by a facile synthesis route, Nanosci. Nanotechnol. Lett. 8 (2016) 434-437.

[24] S.K. Gore, S.S. Jadhav, U.B. Tumberphale, S.M. Shaikh, M. Naushad, R.S. Mane, Cation distribution, magnetic properties and cubic-perovskite phase transition in bismuth-doped nickel ferrite, Solid State Sci.74 (2017) 88-94.

[25] S.U. Bhaskera, Y. Veeraswamy , N. Jayababu , M.V. Ramanareddy, Chromium substitution effect on the structural, optical, electrical and magnetic properties of Nickel ferrite nano

ISSN PRINT 2319 1775 Online 2320 7876

Research paper UGC CARE Listed (Group -I) Journal Volume 11, Iss 8, Dec 2022

particles; synthesized by an environmentally benign auto combustion method, Mater. Today: Proceedings 3 (2016) 3666-3672.

[26] J. Wanga, F. Ren, R. Yi, A. Yan, G. Qiu, X. Liu, Solvothermal synthesis and magnetic properties of size-controlled nickel ferrite nanoparticles, J. Alloys Compd. 479 (2009) 791–796.

[27] S Asiri, Murat Sertkol, S Guner, H Gungunes, KM Batoo, Tawfik A Saleh, H Sozeri, Munirah Abdullah Almessiere, A Manikandan, Abdulhadi Baykal, Hydrothermal synthesis of $Co_yZn_yMn_{1-2y}Fe_2O_4$ nanoferrites: magneto-optical investigation, Ceram. Int. 44 (2018) 5751-5759.

[28] N.A. Algarou, Y. Slimani, M.A. Almessiere, A. Baykal, S. Guner, A. Manikandan, I. Ercan, Enhancement on the exchange coupling behavior of $SrCo_{0.02}Zr_{0.02}Fe_{11.96}O_{19}/MFe_2O_4$ (M= Co, Ni, Cu, Mn and Zn) as hard/soft magnetic nanocomposites, J. Magn. Magn. Mater. 499 (2020) 166308.

[29] M.A. Almessiere, E. Hannachi, Y. Slimani, Ghulam Yasin, M. Mumtaz, M.R. Koblischka, A. Koblischka-Veneva, A. Manikandan, A. Baykal, Dimensionality and superconducting parameters of $YBa_2Cu_3O_{7-d}/(WO_3\ NPs)_x$ composites deduced from excess conductivity analysis, Mater. Chem. Phys. 243 (2020) 122665.

[30] M.A. Almessiere, Y. Slimani, H. Gungunes, M. Nawaz, F.S. Al-ahmari, A. Manikandan, A. Baykal, Investigation of the crystal/magnetic structure, magnetic and optical properties of $SrY_xNb_xFe_{12-2x}O_{19}$ ($x \leq 0.05$) hexaferrites, Phys. Scripta 95 (2020) 055802.

[31] C. Singh, A. Goyal and S. Singhal, Nickel-doped cobalt ferrite nanoparticles: efficient catalysts for the reduction of nitroaromatic compounds and photo-oxidative degradation of toxic dyes, DOI: 10.1039/c4nr01730g.

[32] A. Naduman, K. Shetty, K.S. Anantharaju, H.P. Nagaswarupa, D. Rangappa, Y.S. Vidya, H. Nagabhushana, S.C. Prashantha, Sunlight photocatalytic performance of Mg-doped nickel ferrite synthesized by a green sol-gel route, J. Sci.: Advan. Mater. Devices 4 (2019) 89-100.

[33] Hirthna, S. Sendhilnathan, Enhancement in dielectric and magnetic properties of Mg^{2+} substituted highly porous super paramagnetic nickel ferrite nanoparticles with Williamson-Hall plots mechanistic view, Ceram. Int. 43 (2017) 15447-15453.

[34] P Thilagavathi, A Manikandan, S Sujatha, SK Jaganathan, S Arul Antony, Sol–gel synthesis and characterization studies of $NiMoO_4$ nanostructures for photocatalytic degradation of methylene blue dye, Nanosci. Nanotechnol. Lett. 8 (2016) 438-443.

[35] C.Y. Zhang, X.Q. Shen, J.X. Zhou, M.X. Jing, K. Cao, Synthesis and magnetic properties of nanocomposite $Ni_{1-x}Co_xFe_2O_4$–$BaTiO_3$ fibers by organic gel-thermal decomposition process, J. Sol-Gel Sci. Technol. 42 (2007) 95.

[36] S. Maensiri, C. Masingboon, B. Boonchom and S. Seraphin, A simple route to synthesize nickel ferrite ($NiFe_2O_4$) nanoparticles using egg white, Scripta Materialia 56 (2007) 797-800.

[37] Y. Slimani, M.A. Almessiere, E. Hannachi, A. Baykal, A. Manikandan, M. Mumtaz, F. Ben Azzouz, Influence of WO_3 nanowires on structural, morphological and flux pinning ability of YBa_2Cu_3Oy superconductor, Ceram. Int. 45 (2019) 2621-2628.

ISSN PRINT 2319 1775 Online 2320 7876

Research paper UGC CARE Listed (Group -I) Journal Volume 11, Iss 8, Dec 2022

[38] V. Umapathy, A. Manikandan, S. Arul Antony, P. Ramu, P. Neeraja, Synthesis, structural, morphological and opto-magnetic properties of Bi_2MoO_6 nano-photocatalyst by sol-gel method, Trans. Nonferrous Met. Soc. China 25 (2015) 3271-3278.